

Article

Actin-Myosin Spatial Patterns from a Simplified Isotropic Viscoelastic Model

Owen L. Lewis,¹ Robert D. Guy,¹ and Jun F. Allard^{2,*}¹Department of Mathematics, University of California at Davis, Davis, California; and ²Department of Mathematics, Department of Physics and Astronomy, Center for Complex Biological Systems, University of California at Irvine, Irvine, California

ABSTRACT F-actin networks are involved in cell mechanical processes ranging from motility to endocytosis. The mesoscale architecture of assemblies of individual F-actin polymers that gives rise to micrometer-scale rheological properties is poorly understood, despite numerous *in vivo* and *in vitro* studies. *In vitro* networks have been shown to organize into spatial patterns when spatially confined, including dense spherical shells inside spherical emulsion droplets. Here we develop a simplified model of an isotropic, compressible, viscoelastic material continually assembling and disassembling. We demonstrate that spherical shells emerge naturally when the strain relaxation rate (corresponding to internal network reorganization) is slower than the disassembly rate (corresponding to F-actin depolymerization). These patterns are consistent with recent experiments, including a collapse of shells to a central high-density focus of F-actin when either assembly or disassembly is reduced with drugs. Our results demonstrate how complex spatio-temporal patterns can emerge without spatially distributed force generation, polar alignment of F-actin polymers, or spatially nonuniform regulation of F-actin by upstream biochemical networks.

INTRODUCTION

Actin forms polymers and dynamic networks in most eukaryotic cells (1). These networks are organized with the help of ~130 accessory proteins (2) and have diverse architecture, each tuned for different cell functions including cell motility, division, mechanosensing, endocytosis, receptor-ligand binding, and maintaining cell coherence.

As a key participant in these cellular processes, and a primary determinant of overall cell mechanics (3), the mechanical properties of actin networks have been studied extensively. At the level of individual F-actin polymers, assembly is initiated by nucleators such as Arp2/3, which are activated by membrane-bound nucleation promoting factors such as WASp. Disassembly occurs both spontaneously and under regulation by depolymerization factors such as cofilin. Higher-order actin structures have been studied *in vitro* (4–7), where actin exhibits viscoelastic behavior. Unsurprisingly, given the divergent behaviors seen for *in vivo* actin networks, *in vitro* studies lead to estimates of parameters ranging over orders of magnitude, depending on polymerization setup, accessory molecules, and experimental timescale. For example, reported elastic moduli range in 0.8–30 Pa (4,6,8), small compared to reports of elastic moduli of live cells, which range in 20–40 Pa·s (3,9–12). The network's internal viscosity also exhibits a large range, 10–100 Pa·s *in vitro* (13) to 100–700 Pa·s in live cells (3,9,11,12). In general, a viscoelastic material may not be easily characterized by a single well-defined elastic modulus and viscosity (7).

A major question is, therefore, what are the rheological properties of actin *in vivo*? In particular, what are the relative strengths of elastic stresses, effective viscosity, and myosin contractility? These properties are often necessary in quantitative models of cell processes (14–17), which would benefit from a mathematically simple model of actin-myosin rheology that nevertheless captures key phenomena.

It has been emphasized that acto-myosin constitutes an active, polar, viscoelastic gel (18,19). Although the bulk networks are energetically active and, microscopically, individual filaments are polar, it is unclear whether energetic activity and polarity are essential for explaining nontrivial spatial and temporal patterns observed at cellular scales.

Recently, Pinot et al. (20) reconstituted a dynamic, flowing F-actin network confined in emulsion droplets, shown in Fig. 1 A. The interior of the cell-sized droplets contains extract from meiotic *Xenopus* cells and thus ostensibly represents a full array of *in vivo* actin regulatory protein. In addition, the droplet boundary mimics the cell surface, e.g., recruiting actin nucleation promoting factors. Two curious observations arise from their study:

1. The highest density of actin is neither at the periphery nor the center, but at a concentric sphere, shown in Fig. 1 A, which the authors call “rings” and we refer to as “halos”; and
2. By using drugs that either reduce actin depolymerization (phalloidin) or reduce polymerization (cytochalasin), the halo collapses to a single maximum near the droplet center.

Submitted April 17, 2014, and accepted for publication June 16, 2014.

*Correspondence: jun.allard@uci.edu

Editor: Leah Edelstein-Keshet.

© 2014 by the Biophysical Society
0006-3495/14/08/0863/8 \$2.00



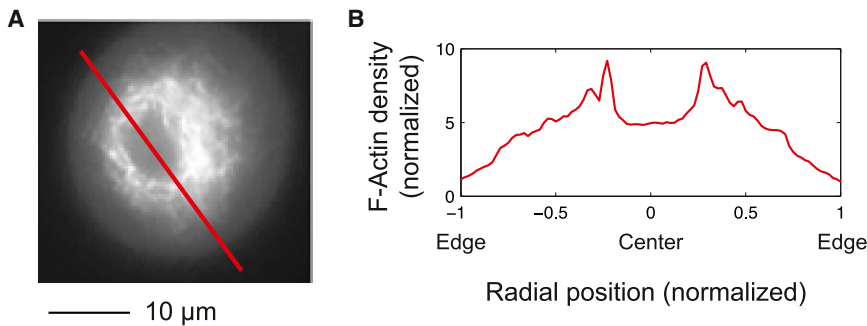


FIGURE 1 F-actin in biomimetic droplets exhibits maximum density at an internal shell. (A) Labeled F-actin in the cytoplasm extracted from meiotic *Xenopus* cells inside emulsion droplets, taken from Pinot et al. (20). (B) Line scan of F-actin intensity (red line in panel A). Background fluorescence was subtracted from the fluorescent intensity and normalized to the intensity at the droplet boundary. To see this figure in color, go online.

This biomimetic system provides a balance between live cell experiments (3,12) in which competing variables such as the cortex, the nucleus, and the larger, actively signaling organelles confound interpretation of experiments, and the in vitro reconstitution (4–7) that may lack physiological significance.

In this work, we propose a simple model and show that the halos and other experimentally observed behaviors can be understood as an interplay among four processes within the network: polymerization, compression, reorganization, and disassembly. Our simple model provides insights of relevance to acto-myosin dynamics in general: We find viscous, elastic, and active contractile stresses have similar magnitudes, although only viscous and elastic stresses are necessary for explaining these halos. Our model adds to a growing body of evidence (21,22) that nontrivial patterns can be generated in simple settings, in this case without invoking polarity or distributed myosin activity.

MODEL

We develop a continuum model that includes the processes depicted in Fig. 2 A: Assembly at the boundary, disassembly throughout the network, network reorganization, and compressional stress due to transient strain. We also include myosin contractility and distributed assembly (not depicted). In the Supporting Material, we provide further mathematical details.

The density of F-actin, a , with units of μM , obeys the evolution equation

$$\frac{\partial a}{\partial t} + \nabla \cdot (\vec{v} a) = -\gamma a + \beta. \quad (1)$$

The left-hand side of the equation corresponds to flow of the F-actin structure due to internal stresses, considered below. The first term on the right-hand side corresponds to depolymerization. The final term represents polymerization in the bulk, which we assume is negligible ($\beta = 0$) for wild-type extract, but can be experimentally induced by the addition of soluble nucleation promoting factors (see Results).

Inertia is negligible and forces must balance, therefore $\nabla \cdot \sigma = 0$, where σ is the total stress with units Pa, which is expressed as

$$\sigma = (\eta(\nabla \vec{v} + \nabla \vec{v}^T) + \eta'(\nabla \cdot \vec{v} \mathbb{I})) - G(e - 1)\mathbb{I} + \sigma_M \mathbb{I}. \quad (2)$$

The three terms above correspond to the viscous, elastic, and active contractile stresses, respectively. The parameter η is the shear viscosity and η' is the second coefficient of viscosity, both with units of $\text{Pa} \cdot \text{s}$, although in spherically symmetric droplets only η impacts our results (see the Supporting Material). G is the bulk elastic modulus with units of Pa, e is the network volumetric strain, and σ_M is the strength of active stresses driven by myosin. Both the elastic and

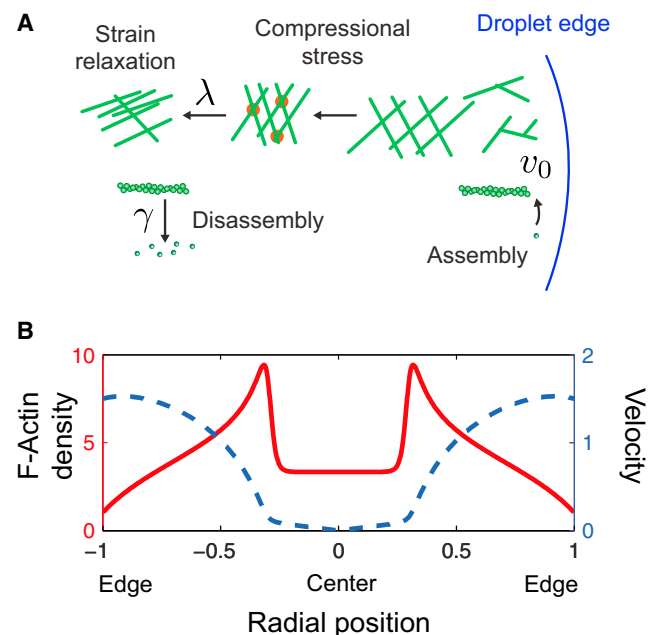


FIGURE 2 Compressible, viscoelastic model demonstrates F-actin interior shell pattern. (A) Schematic of model. F-actin filaments (green) assemble from G-actin monomers, primarily at the droplet edge. F-actin forms a compressible network. Compression leads to strain, which is eventually relaxed with timescale λ as crosslinkers (orange) are recycled. F-actin disassembly occurs throughout the network. (B) F-actin profile (red) and velocity profile (blue) predicted by the model with $\Gamma = 10$, $V_0 = 1.5$, $\alpha = 10^{-2}$, $M = 1$, and $B = 1$. To see this figure in color, go online.

contractile stresses are assumed to be isotropic, and are therefore multiples of the identity tensor \mathbb{I} , an assumption we justify in the [Supporting Material](#).

Because the dynamics of F-actin are on a timescale of minutes ($R_0/v_0 \sim 500$ s), we assume that the forces due to the cytosolic fluid surrounding the F-actin network (which contains solutes including G-actin) are negligible. This allows us to avoid characterizing a full, two-phase model (23) in which the cytosol experiences the F-actin network as a porous medium with timescale ≈ 26 s (24). In the [Supporting Material](#), we derive the equation for volumetric strain, e , as

$$\frac{\partial e}{\partial t} + \nabla \cdot (\vec{v} e) = -\lambda(e - 1). \quad (3)$$

The left-hand side of this equation represents transport of local strain by the velocity of the actin network. The right-hand side represents strain relaxation. The underlying assumption is that the network reorganizes to an unstrained configuration ($e = 1$), and λ is the rate of the associated relaxation of strain within the network. Microscopically, we hypothesize that both strain relaxation (at rate λ) and viscosity (η) are due to the turnover of actin crosslinkers and untangling of filaments. However, even though they involve the same microscopic participants, they are distinct. In our macroscopic model, these processes are distinct because viscous stresses only arise when filaments are moved relative to each other, whereas strain relaxation will occur even if the material is stationary. We use the convention that $e > 1$ corresponds to compression. We assume the elastic modulus, G , scales linearly with actin density:

$$G(a) = g \cdot a/a_0. \quad (4)$$

In Results and [Fig. S1](#) in the [Supporting Material](#), we explore more of the general dependencies between elastic modulus and local F-actin density, including superlinear scaling (4,6,25). We find that all our results are qualitatively the same for superlinear scaling.

The strength of active stresses driven by myosin is

$$\sigma_M = ma. \quad (5)$$

This form assumes myosin contractility is isotropic and proportional to F-actin density (26,27).

Polymerization is observed near the boundary. For simplicity, we assume F-actin is created at constant density a_0 in an unstrained state (see the [Supporting Material](#)), leading to boundary conditions

$$\vec{v}(r_0) = -v_0 \hat{n}, \quad (6)$$

$$a(r_0) = a_0, \quad (7)$$

$$e(r_0) = 1, \quad (8)$$

where v_0 is the F-actin polymerization velocity and \hat{n} is a unit vector normal to the boundary. To test sensitivity to

the assumption of strain-free assembly, we varied strain near the boundary $e(r_0) = 0.1$ and $e(r_0) = 10$, and found negligible effect on flow velocities or the shape of F-actin density profile.

Equations 1–3 with the boundary condition equations, Eqs. 6–8, constitute a system of nonlinear, coupled partial differential equations. To facilitate their numerical solution and intuitive understanding, we perform nondimensionalization (rescaling) by choosing the droplet radius r_0 , strain relaxation time $1/\lambda$, and reference density a_0 as characteristic scales for space, time, and actin density, respectively. We report all findings in terms of $A = a/a_0$ and $V = v/\lambda r_0$, the scaled actin density and velocity, respectively. There are five nondimensional parameters, listed in [Table 1](#). We obtain nondimensional and radially symmetric versions of Eqs. 1–3. To numerically solve these, at every timestep we first use Eq. 2 to solve for the velocity field, and then update actin density and strain fields with Eqs. 1 and 3. Explicit equations and details of numerical methods are presented in the [Supporting Material](#).

RESULTS

Isotropic model with stress reproduces halo pattern

We numerically solve the dynamic equations until they reach a steady-state pattern, shown in [Fig. 2 B](#). Because of droplet-to-droplet variability observed by Pinot et al. (20), our goal is not precise quantitative agreement between our model and any single experimental profiles, but instead to elucidate the mechanical processes that underlie the observed behavior. We are able to reproduce approximate peak location and maximal density and central density relative to edge density, as well as the general character of the profile.

Halo can be understood as competition of F-actin decay and compression resistance

To gain a conceptual understanding of our model's implications, we found numerical solutions over a range of three parameters, α , Γ , and V_0 , corresponding to elastic resistance,

TABLE 1 Nondimensional parameters

Symbol	Definition	Meaning
α	$g/\eta\lambda$	Ratio of elastic to viscous stresses
Γ	γ/λ	Ratio of network decay rate to strain relaxation rate
V_0	$v_0/\lambda r_0$	Ratio of boundary polymerization rate to strain relaxation rate
M	$ma_0/\eta\lambda$	Ratio of active contractile stresses to viscous stresses
B	$\beta/a_0\lambda$	Ratio of bulk polymerization rate to strain relaxation rate

disassembly, and assembly, respectively, with $B = M = 0$ for simplicity. The resulting patterns, shown in Fig. 3, can be understood as follows:

For networks that are completely inelastic ($\alpha = 0$; Fig. 3 A), the formation of actin halos is not possible. The F-actin profile is determined entirely by a competition between assembly and disassembly. If $V_0 > 3\Gamma$ (Fig. 3 (i)), polymerization dominates, the network is driven inward, and actin concentration increases toward the middle. If $V_0 < 3\Gamma$ (Fig. 3 (ii)), network depolymerization dominates and the actin profile decays toward the center. The factor of 3 is a geometric constant that arises in spherical coordinates.

For elastic networks ($\alpha \neq 0$; Fig. 3, B and C), a nontrivial peak generally occurs when $V_0 > 3\Gamma$ and $\Gamma > 1$ (Fig. 3 (iii)). To elucidate the nature of this peak, we explore the stress profile for three parameter sets with only Γ varying (profiles in Fig. 4 correspond to parameters (vi–viii) in Fig. 3).

We find the material separates into two domains: in the outer domain, viscous stresses dominate, whereas in the central domain, elastic stresses dominate. In this central domain, because viscous stresses are small, the elastic stresses must balance either by having constant material (Fig. 4 (vii)), higher density but lower strain (Fig. 4 (viii)), or higher strain but lower density (Fig. 4 (vi)). Which case

prevails is decided by a competition between strain decay (relaxation) and material decay (depolymerization), and is determined solely by $\Gamma = \gamma/\lambda$, the ratio of two decay rates. The latter case, with faster material decay, leads to the peak reported experimentally.

Four experimental perturbations validate model

A counterintuitive result reported by Pinot et al. (20) is that drugs that either reduce actin polymerization (cytochalasin) or reduce depolymerization (phalloidin) result in shell collapse to a single maximum near the droplet center. Our model reproduces this behavior: From the parameter set shown in Fig. 3 (iii), if either Γ or V_0 are reduced (Fig. 3, (iv) and (v), respectively), the peak moves toward the center. Qualitatively, we can understand this behavior as two separate effects. Velocity reduction delays the actin buildup, allowing it to move closer to the center before elastic stresses accumulate. When the depolymerization rate is reduced sufficiently below the strain decay rate, the network relieves elastic stress by reorganization rather than depolymerization, leading to a higher concentration of actin in the center.

Moreover, our model reproduces two other experimental perturbations. When myosin is inhibited (using blebbistatin),

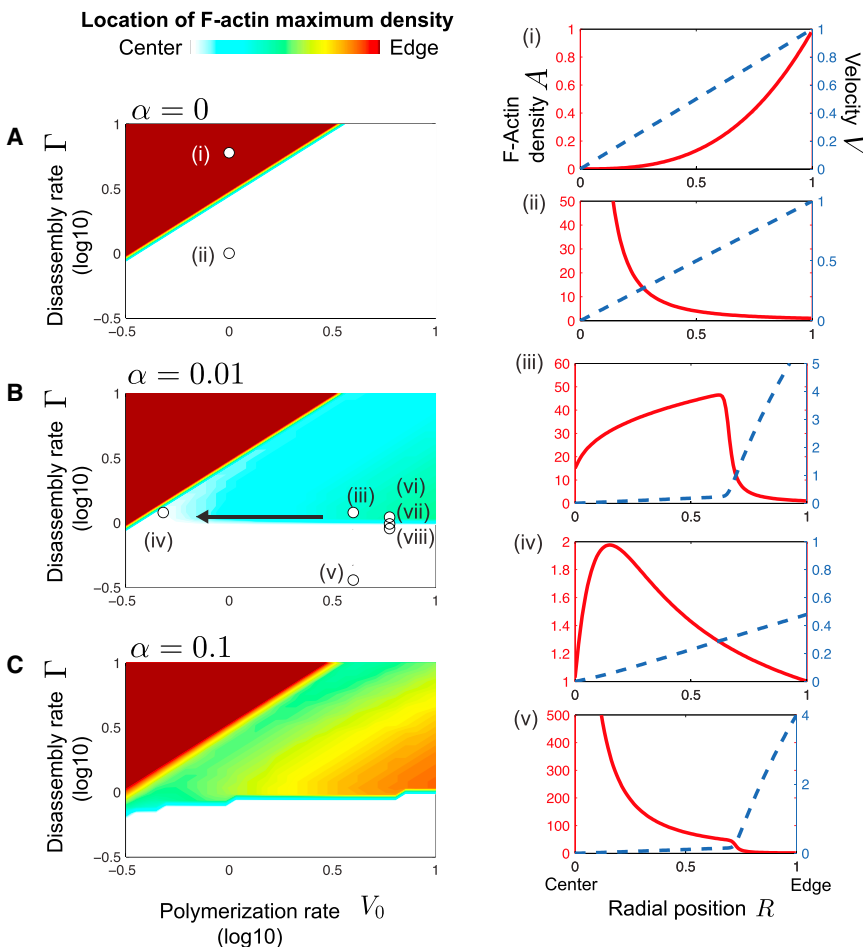


FIGURE 3 (A–C) Location of maximal F-actin density depends on model parameters α , Γ , and V_0 . For simplicity, we set $B = M = 0$. For $\alpha = 0$ (A), F-actin profile either increases toward the middle if $V_0 > 3\Gamma$ (i), or decays if $V_0 < 3\Gamma$ (ii). For nonzero α (B), a nontrivial peak occurs when $V_0 > 3\Gamma$ (iii). From this parameter set, if either Γ or V_0 are reduced ((iv) and (v), respectively), the peak moves toward the center. (vi–viii) Correspond to parameters shown in Fig. 4. To see this figure in color, go online.

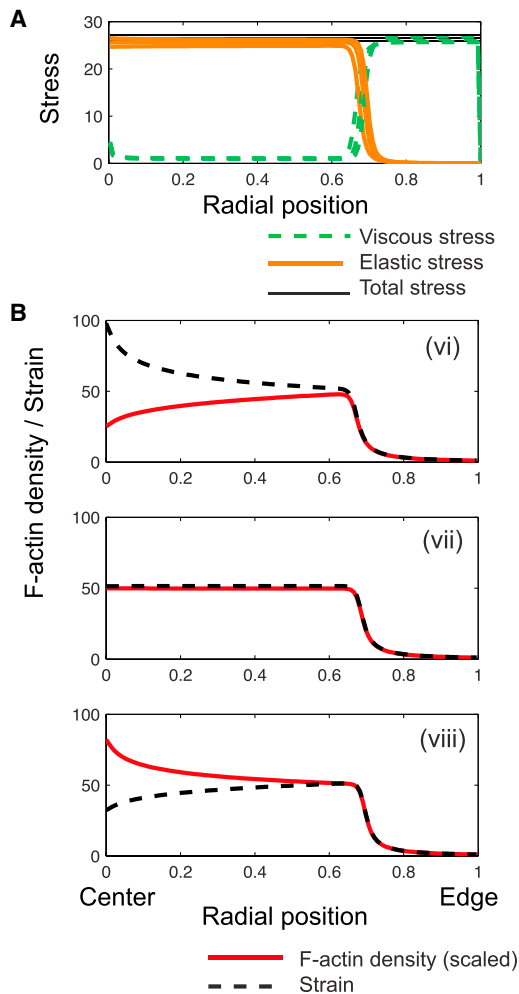


FIGURE 4 (A) Elastic resistance leads to domain separation of primarily viscous stress (orange) near the edge and primarily elastic stress near the center (green), computed using the first and second terms in Eq. 2. Total stress (black) is constant throughout the material, as required by force-balance. (B) The switch from viscous to elastic stress corresponds to the peak in F-actin (vi). This peak results from a competition between strain decay (relaxation) and material decay (disassembly): if $\Gamma > 1$ ($\lambda < \gamma$) as in (vi), F-actin decays toward the center, resulting in an F-actin density peak. If $\Gamma < 1$ ($\lambda > \gamma$) as in (viii), strain decays toward the center, which is compensated by increasing F-actin density. To see this figure in color, go online.

the flow velocity is reduced by $\sim 30\%$. We varied the myosin contractility parameter M to find what value perturbs the velocity profile by this amount, shown in Fig. 5 A. We find that from $M = 1$ to $M = 0$, the velocity profile changes by approximately one-third, giving a rough order-of-magnitude estimate that $M \sim 1$. If $M > 10$, the flow velocity reverses sign inside the shell. This reversal is driven by a positive feedback loop built into our model: Contractility tends to concentrate actin, and higher concentrations of actin lead to higher concentrations of myosin, furthering contraction. Our model thus predicts that large enough myosin contractility will reverse the flow inside the ring, directing it outward.

Pinot et al. (20) engineered a diffusible actin nucleation promoting factor called Scar-WA. The addition of such

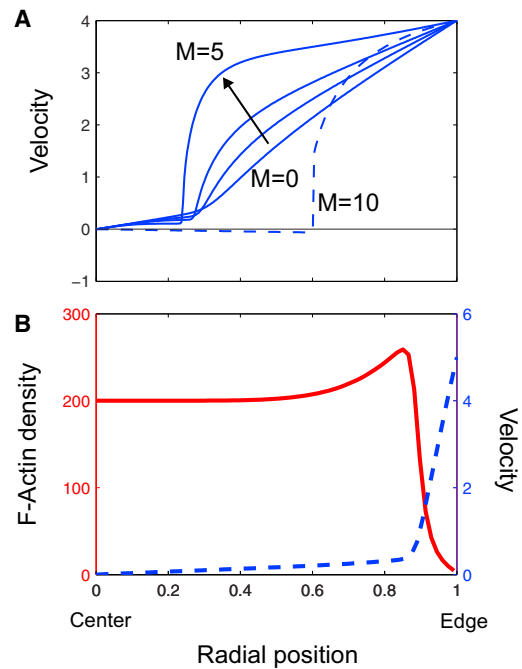


FIGURE 5 (A) Myosin contractility increases flow velocity, until myosin is strong enough to reverse the flow. Numerical solutions computed for $M = 0, 1, 2, 5$ (blue solid lines) and $M = 10$ (dashed line). Note in this plot, $V > 0$ corresponds to inward flow, and $V < 0$ is outward flow. The resulting F-actin density profiles (not shown) become increasingly more sharply peaked. (B) Distributed F-actin assembly leads to an approximately uniform density profile. To see this figure in color, go online.

distributed F-actin assembly led to a uniform density of F-actin, with apparent lower density near the edges (although this may be due to microscopy effects). Our model with distributed assembly $\beta > 0 \rightarrow B > 0$ recapitulates this result, shown in Fig. 5 B.

Model is robust to elastic modulus scaling with F-actin density

Measurements of in vitro F-actin networks have reported the scaling between elastic modulus and F-actin density as $G \sim a^{7/5}$ (4) and $G \sim a^{11/5}$ (25). To test whether our results are robust to the scaling law, we explore dependencies that are more general between elastic modulus and local F-actin density, including superlinear scaling $G \sim a^{7/5}$. We find that all our results are qualitatively the same for superlinear scaling. To further explore the importance of the density dependence, we simulated constant G (independent of actin density a) and were unable to reproduce assembly/disassembly perturbation experiments.

Dynamics without spherical symmetry and merging droplets

The viscoelastic model we propose can be generalized to higher dimensions without imposing spherical symmetry.

To explore the behavior without imposed symmetry, we solve the model equations in a two-dimensional square with F-actin assembly on the four straight edges. We find a large regime of parameters result in steady states with halo structures. An example steady state for $\alpha = 0.1$, $\Gamma = 2.5$, $V_0 = 1$, and $M = B = 0$ is shown in Fig. 6 and Movie S1 in the Supporting Material. Fourfold symmetry in the halo intensity is an artifact of our square boundary.

When two droplets, each containing an F-actin halo, contact each other, surface tension induces a rapid merger into a single oil droplet. After the droplet merging, the F-actin halos merge into a single halo with a merging timescale of minutes. We explore the dynamics predicted by our viscoelastic model during network merging. To separate the physics of the droplet merger, which is beyond the scope of this work, with the physics of F-actin network merger, we simulate in rectangular geometry. We first find the steady state of an individual network confined to a square with edge length $r_0/2$ at parameters that produce halo patterns. We then simulate a larger square with edge length r_0 and use as initial condition two identical copies of the smaller halo, shown in Fig. 6, $t = 0$. The resulting merger is shown in Movie S2.

These simulations demonstrate the following:

1. Our results qualitatively carry over to different dimensions and symmetry assumptions; e.g., we did not detect instabilities in circumferential directions, and
2. The halos are not metastable, and merge into a single halo on a timescale comparable to the timescale of halo merger reported experimentally.

DISCUSSION

F-actin networks are complex materials, exhibiting phenomena depending on at least five properties:

1. They are viscoelastic (10);
2. They continually assemble and disassemble;
3. Both polymerization and depolymerization generate force throughout the network (28);
4. In general, the polarity of individual polymers can lead to anisotropic network behavior; and
5. The network is under spatially nonuniform regulation by an upstream biochemical networks (29).

The primary result of this work is that nontrivial spatial patterns can arise only from properties 1 and 2. These critical

features are consistent with a large class of constitutive laws, and are not limited to our specific functional form. For example, polarity (18,27) and more-complex viscous and elastic constitutive laws may be included; but with our four basic ingredients, we expect halo formation.

We observe the emergence of halo patterns, in which the maximal F-actin density is neither at the boundary nor in a single focus, but rather in a spherical shell. The phase diagrams in Fig. 3 lead to a conceptual description of halo formation under two conditions:

1. If assembly dominates over disassembly, the network must become more dense as it flows inward from the boundary, thus the maximal density will not be at the boundary; and
2. A competition arises between the timescale of material strain decay (the viscoelastic timescale) and material decay (F-actin depolymerization).

If material decay is faster than material strain decay, the network depolymerizes at the center but strain increases. In Fig. S1, we show that the dimensionality and precise geometry are unimportant by solving the equations in a one-dimensional strip, where we find qualitatively similar behavior. The phase diagrams also recapitulate the counterintuitive observation that the halo pattern collapses to a central focus under either cytochalasin, which decreases F-actin assembly, or phalloidin, which decreases disassembly. Conceptually, the cytochalasin collapse results from a competition between assembly and disassembly, whereas the phalloidin collapse results from competition between disassembly and strain decay.

Although flow velocities and network densities can be observed directly in experiment, internal stress and strain remains difficult to measure in bulk content of cells and in vitro networks. Thus, one benefit of mathematical models is their ability to relate observable network properties to these unobservable properties. Here, the major conclusion from our model is that the internal stress in the F-actin network in Pinot et al. (20) is approximately evenly shared between elastic stress, viscous stress, and myosin contractile stress. These stresses are, however, not uniformly shared in space. Instead, we predict the stress is predominantly viscous in an outer region (outside the halo) and predominantly elastic in an inner region (within the halo), as shown in Fig. 4.

The simplicity of our nondimensional model equations allows description of spatial patterns and the effect of

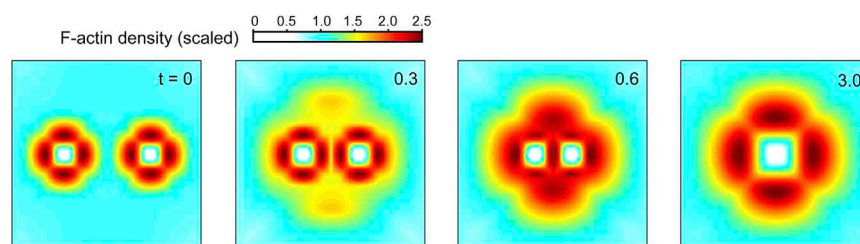


FIGURE 6 F-actin density from a two-dimensional simulation of actin confined inside a square with assembly on the outer edges. Time sequence of F-actin density profiles as two steady-state halos are placed in a larger square domain. The final frame shows steady state. Time is in scaled units of the strain relaxation time λ^{-1} . Fourfold symmetry is an artifact of the square boundary. To see this figure in color, go online.

drug perturbations without specifying precise values of rheological parameters, for which quantitative values remain elusive (see Introduction). However, connecting qualitative features of halos with our model allows for inference of parameters. The strain relaxation rate λ is related to the reorganization timescale of the F-actin network, itself related to the kinetics of F-actin cross-linking proteins such as filamin and fascin (6–8). This timescale also determines the characteristic scale above which the network may be assumed to be approximately fluidlike, and below which the network is primarily elastic, and has been estimated to be 0.1–10 s in cells and 10–100 s in vitro when crosslinked by ADP-myosin (13). Our model suggests that the network in Pinot et al. (20) has a strain relaxation time slightly below the disassembly time γ , which is straightforward to observe experimentally, for example with fluorescence recovery after photobleaching (30).

Nonetheless, we expect our nondimensional parameters to be consistent with the range of reported (physical) parameters. The behavior we report occurs over a range of nondimensional parameters, including $\alpha \sim 10^{-1}$, $\Gamma \sim 10$, and $V_0 \sim 10^{-1}$. Among many possibilities, these parameters are consistent with $\lambda \sim 0.1 \text{ s}^{-1}$, $\gamma \sim 1 \text{ s}^{-1}$ (see previous paragraph), $\eta \sim 10^3 \text{ Pa}\cdot\text{s}$ (3,9,11,12), and G ranging from 10 Pa at the boundary to 100 Pa at maximal density (3,9–12), assuming $R_0 = 25 \text{ }\mu\text{m}$ and $v_0 = 250 \text{ nm/s}$.

We have developed a simple continuum model of a compressible viscoelastic material with assembly/disassembly. The material we describe is similar to Oldroyd-B and upper-convected Maxwell materials because it has fluid behavior at long timescales, and an effective memory at intermediate timescales. These models have been extended to allow for compressibility (31–33). Our model equations are simple enough to allow for efficient numerical solution over a large parameter regime: in the case of no myosin or distributed assembly, the model has three nondimensional parameters that we characterize completely (Fig. 3). In addition, it is straightforward to add more complex assembly and disassembly kinetics by modifying Eq. 1.

Relatively recent experiments (34,35) and theories (28,36) have demonstrated that disassembly can generate stress, including at the rear of motile cells. This could be included in our modeling framework as a term in the stress equation, e.g., $\sigma = +E(a - a_1)$, $a > a_1$, where a_1 is the preferred density and the positive sign indicates a contractile stress. Full exploration of disassembly stress is beyond the scope of this work. However, we speculate it would not be sufficient to generate halos because the stress would decay at the F-actin disassembly rate; we find that halos emerge only when the material disassembly rate and stress decay rate are different.

Previous experiments (4,37,38) demonstrate that stabilized (depolymerization inhibited) F-actin confined in droplets or vesicles form rings when the diameter of the ring was below the persistence length of the filaments ($\sim 15 \text{ }\mu\text{m}$). We

hypothesize that these patterns emerge from distinct mechanisms from the halos reported by Pinot et al. (20), because of the following:

1. The oil droplets are much larger, with diameters $\sim 100 \text{ }\mu\text{m}$, sizes at which rings were not observed in previous experiments (4,37,38);
2. The halos are consistently not at the confinement boundary in Pinot et al. (20), whereas most rings occurred at the confinement boundary (with exceptions (38)); and
3. The phalloidin and cytochalasin-D experiments in Pinot et al. (20) demonstrate these halos depend on continual, unperturbed assembly and disassembly.

Our model makes several testable predictions, including the flow profiles shown Fig. 2 (blue dashed curve) and how they vary under experimental perturbations. By increasing myosin contractility strength, we predict that above a threshold strength, the F-actin peak density (i.e., the halo's location in the droplet) will move out, and at this myosin strength, the flow inside the halo will reverse direction. This prediction could be tested with drugs that increase myosin contractility, e.g., calyculin A.

SUPPORTING MATERIAL

One figure, additional supplemental information and two movies are available at [http://www.biophysj.org/biophysj/supplemental/S0006-3495\(14\)00687-0](http://www.biophysj.org/biophysj/supplemental/S0006-3495(14)00687-0).

This work was supported in part by National Science Foundation grants No. DMS-1160438 and No. DMS-1226386 to R.D.G.

SUPPORTING CITATIONS

References (39,40) appear in the [Supporting Material](#).

REFERENCES

1. Pollard, T. D., and J. A. Cooper. 2009. Actin, a central player in cell shape and movement. *Science*. 326:1208–1212.
2. Ditlev, J. A., B. J. Mayer, and L. M. Loew. 2013. There is more than one way to model an elephant. Experiment-driven modeling of the actin cytoskeleton. *Biophys. J.* 104:520–532.
3. Ketene, A. N., P. C. Roberts, ..., M. Agah. 2012. Actin filaments play a primary role for structural integrity and viscoelastic response in cells. *Integr. Biol. (Camb.)*. 4:540–549.
4. Claessens, M. M. A. E., R. Tharmann, ..., A. R. Bausch. 2006. Microstructure and viscoelasticity of confined semiflexible polymer networks. *Nat. Phys.* 2:186–189.
5. Reymann, A.-C., R. Boujemaa-Paterski, ..., L. Blanchoin. 2012. Actin network architecture can determine myosin motor activity. *Science*. 336:1310–1314.
6. Koenderink, G. H., Z. Dogic, ..., D. A. Weitz. 2009. An active biopolymer network controlled by molecular motors. *Proc. Natl. Acad. Sci. USA*. 106:15192–15197.
7. Mizuno, D., C. Tardin, ..., F. C. Mackintosh. 2007. Nonequilibrium mechanics of active cytoskeletal networks. *Science*. 315:370–373.
8. Lieleg, O., J. Kayser, ..., A. R. Bausch. 2011. Slow dynamics and internal stress relaxation in bundled cytoskeletal networks. *Nat. Mater.* 10:236–242.

9. Moreno-Flores, S., R. Benitez, ..., J. L. Toca-Herrera. 2010. Stress relaxation and creep on living cells with the atomic force microscope: a means to calculate elastic moduli and viscosities of cell components. *Nanotechnology*. 21:445101.
10. Yamada, S., D. Wirtz, and S. C. Kuo. 2000. Mechanics of living cells measured by laser tracking microrheology. *Biophys. J.* 78:1736–1747.
11. Bausch, A. R., W. Möller, and E. Sackmann. 1999. Measurement of local viscoelasticity and forces in living cells by magnetic tweezers. *Biophys. J.* 76:573–579.
12. Bausch, A. R., F. Ziemann, ..., E. Sackmann. 1998. Local measurements of viscoelastic parameters of adherent cell surfaces by magnetic bead microrheometry. *Biophys. J.* 75:2038–2049.
13. Norstrom, M., and M. L. Gardel. 2011. Shear thickening of F-actin networks crosslinked with non-muscle myosin IIB. *Soft Matter*. 2011:3228–3233.
14. Rubinstein, B., M. F. Fournier, ..., A. Mogilner. 2009. Actin-myosin viscoelastic flow in the keratocyte lamellipod. *Biophys. J.* 97:1853–1863.
15. Kim, J. S., C.-H. Lee, ..., P. A. Coulombe. 2012. Mathematical modeling of the impact of actin and keratin filaments on keratinocyte cell spreading. *Biophys. J.* 103:1828–1838.
16. Craig, E. M., D. van Goor, ..., A. Mogilner. 2012. Membrane tension, myosin force, and actin turnover maintain actin treadmill in the nerve growth cone. *Biophys. J.* 102:1503–1513.
17. Shao, D., W. J. Rappel, and H. Levine. 2010. Computational model for cell morphodynamics. *Phys. Rev. Lett.* 105:108104.
18. Joanny, J. F., and J. Prost. 2009. Active gels as a description of the actin-myosin cytoskeleton. *HFSP J.* 3:94–104.
19. Ramaswamy, S. 2010. The mechanics and statistics of active matter. *Annu. Rev. Cond. Mat. Phys.* 1:323–345.
20. Pinot, M., V. Steiner, ..., Z. Gueroui. 2012. Confinement induces actin flow in a meiotic cytoplasm. *Proc. Natl. Acad. Sci. USA.* 109:11705–11710.
21. Bois, J. S., F. Jülicher, and S. W. Grill. 2011. Pattern formation in active fluids. *Phys. Rev. Lett.* 106:028103.
22. Howard, J., S. W. Grill, and J. S. Bois. 2011. Turing's next steps: the mechanochemical basis of morphogenesis. *Nat. Rev. Mol. Cell Biol.* 12:392–398.
23. Herant, M., and M. Dembo. 2010. Form and function in cell motility: from fibroblasts to keratocytes. *Biophys. J.* 98:1408–1417.
24. Charras, G. T., T. J. Mitchison, and L. Mahadevan. 2009. Animal cell hydraulics. *J. Cell Sci.* 122:3233–3241.
25. MacKintosh, F. C., J. Käs, and P. A. Janmey. 1995. Elasticity of semi-flexible biopolymer networks. *Phys. Rev. Lett.* 75:4425–4428.
26. Barnhart, E. L., K.-C. Lee, ..., J. A. Theriot. 2011. An adhesion-dependent switch between mechanisms that determine motile cell shape. *PLoS Biol.* 9:e1001059.
27. Kruse, K., J. F. Joanny, ..., K. Sekimoto. 2005. Generic theory of active polar gels: a paradigm for cytoskeletal dynamics. *Eur. Phys. J. E Soft Matter*. 16:5–16.
28. Mogilner, A., and G. Oster. 2003. Cell biology. Shrinking gels pull cells. *Science*. 302:1340–1341.
29. Welch, C. M., H. Elliott, ..., K. M. Hahn. 2011. Imaging the coordination of multiple signaling activities in living cells. *Nat. Rev. Mol. Cell Biol.* 12:749–756.
30. Smith, M. B., T. Kiuchi, ..., D. Vavylonis. 2013. Distributed actin turnover in the lamellipodium and FRAP kinetics. *Biophys. J.* 104:247–257.
31. Keshtiban, I. J., F. Belblidia, and M. F. Webster. 2004. Numerical simulation of compressible viscoelastic liquids. *J. Non-Newt. Fluid Mech.* 122:131–146.
32. Sureshkumar, R. 2004. Stability analysis using compressible viscoelastic formulation. *J. Non-Newt. Fluid Mech.* 116:471–477.
33. Guillopé, C., and R. Talhouk. 2003. Steady flows of slightly compressible viscoelastic fluids of Jeffreys' type around an obstacle. *Differ. Integr. Eq.* 16:1293–1320.
34. Mseka, T., and L. P. Cramer. 2011. Actin depolymerization-based force retracts the cell rear in polarizing and migrating cells. *Curr. Biol.* 21:2085–2091.
35. Shimabukuro, K., N. Noda, ..., T. M. Roberts. 2011. Reconstitution of amoeboid motility in vitro identifies a motor-independent mechanism for cell body retraction. *Curr. Biol.* 21:1727–1731.
36. Zajac, M., B. Dacanay, ..., C. W. Wolgemuth. 2008. Depolymerization-driven flow in nematode spermatozoa relates crawling speed to size and shape. *Biophys. J.* 94:3810–3823.
37. Limozin, L., M. Bärmann, and E. Sackmann. 2003. On the organization of self-assembled actin networks in giant vesicles. *Eur. Phys. J. E Soft Matter*. 10:319–330.
38. Limozin, L., and E. Sackmann. 2002. Polymorphism of cross-linked actin networks in giant vesicles. *Phys. Rev. Lett.* 89:168103.
39. Doghri, I. 2000. *Mechanics of Deformable Solids: Linear, Nonlinear, Analytical and Computational Aspects*. Springer, New York.
40. Harlow, F. H., and J. E. Welch. 1965. Numerical calculation of time-dependent viscous incompressible flow of fluid with free surface. *Phys. Fluids*. 8:2182–2189.

Actin-myosin spatial patterns from a simplified isotropic viscoelastic model

Owen L. Lewis[†], Robert D. Guy,[†] and Jun Allard^{‡*}

[†]Department of Mathematics, University of California, Davis, [‡]Department of Mathematics, Department of Physics and Astronomy, Center for Complex Biological Systems, University of California, Irvine, *Corresponding author

Supplemental Text

Derivation of viscoelastic model

Derivation of Elastic Stresses within Actin Network We begin by noting that all flows observed in [1] are directed radially inward. Thus we make the simplifying assumption that there is no shear contribution to elastic stress, $\boldsymbol{\sigma}_E$. We formulate an elastic stress law that depends only on local volume changes within the actin network and as mentioned, is isotropic in nature. Thus, our form of the elastic stress is

$$\boldsymbol{\sigma}_e = G(1 - e)\mathbb{I}, \quad (1)$$

where G is a material parameter (that may depend on actin concentration a) and e is our measure of local volume changes, defined as

$$e(x, t) = J^{-1}, \text{ where } J = \det(\mathbf{F}). \quad (2)$$

Here, $\mathbf{F} = \partial\vec{x}/\partial\vec{S}$ is the deformation gradient tensor, \vec{x} is the Eulerian coordinate description of the actin network, and \vec{S} is the Lagrangian reference coordinate. We refer to the quantity $1 - e$ as the “volumetric strain”. A negative strain ($e > 1$) corresponds to a compressed material, while a positive strain ($e < 1$) indicates a material in an expanded state.

To derive equation (1) via the theory of hyper-elastic materials, we define the material properties of the network by choice of an elastic energy density functional. We choose

$$W(\mathbf{F}) = G (J - \ln(J) - 1). \quad (3)$$

The first Kirchoff-Piola stress tensor is given by the derivative of elastic strain energy density

$$\mathbf{P}_{ij} = \frac{\partial W}{\partial \mathbf{F}_{ij}}. \quad (4)$$

From our chosen elastic energy function (3), we calculate

$$\mathbf{P} = G \left(1 - \frac{1}{J} \right) J \mathbf{F}^{-T}. \quad (5)$$

Here we have used the identity that

$$\frac{\partial J}{\partial \mathbf{F}} = J \mathbf{F}^{-T} \quad (6)$$

In general, the Cauchy stress is given by $\boldsymbol{\sigma}_E = J^{-1} \mathbf{P} \mathbf{F}^T$, which in the context of our model gives

$$\boldsymbol{\sigma}_E = G \frac{1}{J} (J - 1) \mathbb{I} = G (1 - e) \mathbb{I}, \quad (7)$$

which is the elastic stress tensor in equation (1).

In a commonly used formulation of neo-Hookean elasticity, the elastic energy associated with material volume changes is given by $W = \frac{\kappa}{2} (J - 1)^2$ [2]. A Taylor expansion of of this standard energy for small deformations (where $J = 1 + \varepsilon$) yields

$$W \approx \kappa \varepsilon^2 \quad (8)$$

Similarly, an expansion of our proposed energy function (3) yields

$$W(J) \approx G \varepsilon^2. \quad (9)$$

Thus, we see that our model of the network elastic energy agrees with commonly used for models for small deformation. The material parameter G is equivalent to the bulk elastic modulus.

For large deformations, our elastic energy functional, equation (3), diverges for $J \leq 0$. Intuitively, this corresponds to an infinite compression that

would require infinite energy (and stress) to achieve. This feature may be desirable, and is not present in standard neo-Hookean treatments. However we note that in the limit of very high stress, the F-actin network may break apart and the continuum elastic description may no longer be appropriate.

The bulk modulus $G(a)$ has an as-yet unspecified dependence on the actin density a . Following theoretical and experimental evidence, we consider three possibilities:

1. Linear scaling $G(a) = g \cdot (a/a_0)$,
2. Super-linear scaling: $G(a) = g \cdot (a/a_0)^{5/2}$,
3. Independence from actin density: $G = g \neq G(a)$.

In the main text of this work, we report results assuming Case (1). We found that assuming Case (2) does not qualitatively affect the predictions of the model (see Supplemental Figure 1). However, Case (3) does qualitatively affect the model, as it does not allow for the formation of actin halos (see Supplemental Figure 1).

Evolution of scalar strain measurement We now derive the evolution equation of our measure of volume change e . Beginning from the definition of J , we have

$$J(\vec{S}, t) = \det \left(\frac{\partial \vec{x}}{\partial \vec{S}} (\vec{S}, t) \right). \quad (10)$$

Applying the chain rule and mapping to Eulerian coordinates, we derive the expression

$$\frac{\partial}{\partial t} J + \vec{v} \cdot \nabla J = (\nabla \cdot \vec{v}) J. \quad (11)$$

Here we have used the identity that

$$\frac{d}{dt} \det(\mathbf{F}) = \det(\mathbf{F}) \operatorname{tr} \left(\mathbf{F}^{-1} \frac{d\mathbf{F}}{dt} \right). \quad (12)$$

Now recall that our quantity of interest is $e = J^{-1}$. Therefore, we have

$$\frac{\partial e}{\partial t} = -J^{-2} \frac{\partial J}{\partial t} = J^{-2} \vec{v} \cdot \nabla J - (\nabla \cdot \vec{v}) J^{-1}. \quad (13)$$

We now notice that the right hand side of this expression is a full derivative, and thus

$$\frac{\partial e}{\partial t} = -\nabla \cdot (\vec{v}J^{-1}). \quad (14)$$

This leads us to the transport equation

$$\frac{\partial e}{\partial t} + \nabla \cdot (\vec{v}e) = 0. \quad (15)$$

Recall that the network of F-actin is not perfectly elastic, but rather has a characteristic timescale during which filaments reorganize in the bulk. Thus, we make the assumption that our measure of strain has a characteristic timescale of elastic memory. For simplicity we assume linear decay of strain towards the unstrained state ($e = 1$):

$$\frac{\partial e}{\partial t} + \nabla \cdot (\vec{v}e) = \lambda(1 - e). \quad (16)$$

The parameter λ we refer to as the strain relaxation rate. To ensure our results are not sensitive to the assumption of linear decay of e , in Supplemental Figure 1 we simulate the model with a quadratic decay term. We find this does not qualitatively affect the results.

Boundary conditions and biophysics of actin interaction with surface Several unknown biophysical properties of the present F-actin structure obfuscate specifying the boundary conditions, including polymerization kinetics, which depends on G-actin concentration and other unknown quantities such as the surface tension of the droplet. However, a simplifying assumption allows full specification: At the boundary, stresses are low relative to the actin polymerization stall forces $\sigma/\rho \ll F_{\text{stall}}$ where ρ is the barbed-end density, and relative to the elastic modulus $\sigma \ll G$. Then

$$\vec{v}|_{\partial\Omega} = v_0\hat{r} \quad (17)$$

$$a|_{\partial\Omega} = a_0 \quad (18)$$

where v_0 is the F-actin free velocity. Two observations lend support to this assumption: The relatively large velocities reported by [1] in steady state relative to F-actin in lamellipodia of motile cells, which evidence suggests are not force-limited, and the relatively low density of actin in the fluorescence images of [1]. In this case, the flux of newly-polymerized actin is fixed,

$av = a_0v_0$. Finally, we assume that newly-polymerized actin network is created in the “preferred” state, and thus our measure of strain will be unity:

$$e|_{\partial\Omega} = 1 \quad (19)$$

Analysis of model equations

Spherical symmetry When simulating conditions in which approximate spherical symmetry is exhibited by the F-actin network, we impose spherical symmetry to reduce the calculation to one spatial coordinate, r . We also assume that the velocity field \vec{v} has only a radial component. This is to say $\vec{v} = v(r)\hat{r}$. In this case, the force balance equation which defines the actin velocity reduces to

$$0 = (2\eta + \eta') \left(\frac{1}{r^2} \frac{\partial}{\partial r} \left(r^2 \frac{\partial v}{\partial r} \right) - \frac{2v}{r^2} \right) + \frac{\partial}{\partial r} (g(a/a_0)^\nu (1 - e) + ma), \quad v|_{\partial\Omega} = v_0. \quad (20)$$

Thus, it can be seen that under the assumption of spherical symmetry, effects due to the shear viscosity η and the second viscosity η' are indistinguishable. The stress due to viscous effects is characterized by a single parameter which we call the “effective viscosity” $\bar{\eta} = 2\eta + \eta'$. In the main text of this work, we will often denote the effective viscosity as η for simplicity.

We perform non-dimensionalization (re-scaling) of the model by choosing the droplet radius r_0 , strain relaxation time $1/\lambda$ and reference actin densities a_0 as characteristic scales for space, time and actin density respectively, leading to

$$0 = \frac{1}{R^2} \frac{\partial}{\partial R} \left(R^2 \frac{\partial V}{\partial R} \right) - \frac{2V}{R} + \frac{\partial}{\partial R} (\alpha A^\nu (1 - e) + MA), \quad V|_{\partial\Omega} = V_0 \quad (21)$$

$$\frac{\partial A}{\partial T} = -\frac{1}{R^2} \frac{\partial}{\partial R} (R^2 VA) + B - \Gamma A, \quad A|_{\partial\Omega} = 1 \quad (22)$$

$$\frac{\partial e}{\partial T} = -\frac{1}{R^2} \frac{\partial}{\partial R} (R^2 Ve) + 1 - e, \quad e|_{\partial\Omega} = 1 \quad (23)$$

where $A = a/a_0$ and $V = v/\lambda r_0$ are the scaled actin density and velocity and

there are five nondimensional model parameters,

$$\alpha = g/\eta\lambda a_0, \quad (24)$$

$$\Gamma = \gamma/\lambda, \quad (25)$$

$$V_0 = v_0/\lambda r_0, \quad (26)$$

$$M = m/\eta\lambda \quad (27)$$

$$B = \beta/a_0\lambda. \quad (28)$$

The elastic modulus scaling law is set by $\nu = 0, 1$ or $5/2$ for independent, linear and super-linear scaling.

Rectangular coordinates When performing simulations of merging droplets, or demonstrating the independence of model predictions from the imposed geometry, we simulate the model equations in a 2-dimensional square domain. In this context, the force balance equation becomes

$$0 = \eta (\Delta \vec{v} + \nabla \cdot \nabla \vec{v}) + \eta' \nabla \cdot \nabla \vec{v} + \nabla (g(a/a_0)^\nu (1 - e)) + \nabla (ma), \quad \vec{v}|_{\partial\Omega} = \vec{v}_0 \quad (29)$$

For our 2-D simulations, we make the simplifying assumption that the second coefficient of viscosity is equal and opposite to the shear viscosity ($\eta' = -\eta$). This is equivalent to assuming that the network has zero bulk viscosity.

Performing non-dimensionalization of the model equations using r_0 , $1/\lambda$ and a_0 as before, we arrive at the following:

$$0 = \Delta \vec{V} + \nabla (\alpha A^\nu (1 - e)) + \nabla (MA), \quad \vec{V}|_{\partial\Omega} = \vec{V}_0 \quad (30)$$

$$\frac{\partial A}{\partial T} = -\nabla \cdot (\vec{V}A) + B - \Gamma A \quad A|_{\partial\Omega} = 1 \quad (31)$$

$$\frac{\partial e}{\partial T} = -\nabla \cdot (\vec{V}e) + 1 - e \quad e|_{\partial\Omega} = 1 \quad (32)$$

In the 2-D domain, we relax the assumption that the boundary velocity is in the normal direction to the boundary. In order to mimic the radially symmetric case, we impose a constant boundary condition on the velocity that is directed radially inward toward the center of the domain

$$\vec{V}_0 = \frac{V_0 (\hat{x} + \hat{y})}{\sqrt{x^2 + y^2}}. \quad (33)$$

Details of numerical simulation

Radially Symmetric Geometry

Due to the form of equations (22) and (23), it is advantageous to use a finite volume numerical method. Due to the radial symmetry of the problem, our control volumes will be concentric spherical shells. This will result in a staggered discretization of the domain $0 \leq r \leq 1$ with spacing ΔR which defines N control volumes $(\{\Omega_n\}_{n=1}^N)$. The boundaries of the control volumes correspond to an edge centered grid given by

$$\{R_n^e\}_{n=1}^N = \{(n - 1/2) \Delta R\}_{n=1}^N. \quad (34)$$

The ‘‘centers’’ of each spherical shell control volume correspond to a cell centered mesh given by

$$\{R_n^c\}_{n=1}^N = \{(n - 1) \Delta R\}_{n=1}^N. \quad (35)$$

Now, approximate the actin concentration within any control volume with

$$A_n = \frac{1}{|\Omega_n|} \int_{\Omega_n} A dV \approx A(R_n^c). \quad (36)$$

Integrating (22) over control volume Ω_n , dividing by $|\Omega_n|$ and rearranging, we have

$$\frac{\partial A_n}{\partial t} = -\frac{1}{|\Omega_n|} \int_{\Omega_n} \nabla \cdot (\vec{V} A) dV + B - \Gamma A_n. \quad (37)$$

Exploiting the spherical symmetry of \vec{V} and the divergence theorem, we have

$$\frac{\partial A_n}{\partial t} = \frac{1}{|\Omega_n|} (|\partial\Omega_n^+| \mathcal{F}_A^{n+} - |\partial\Omega_n^-| \mathcal{F}_A^{n-}) + B - \Gamma A_n. \quad (38)$$

Here $|\partial\Omega_n^+|$ and $|\partial\Omega_n^-|$ are the surface areas of the outer and inner boundaries of Ω_n respectively. \mathcal{F}_A^{n+} and \mathcal{F}_A^{n-} are the flux of actin through $\partial\Omega_n^+$ and $\partial\Omega_n^-$, which by our assumption of radial symmetry are constant over each boundary. The flux through a control volume boundary is given by

$$\mathcal{F}_A^{n+} = A_n^* V_n, \quad (39)$$

where V_n is the velocity through $\partial\Omega_n^+$ and A_n^* is the appropriately chosen ‘‘upstream’’ actin density. To evolve this equation in time, the flux difference

term is treated explicitly with a first order unwinding scheme, while all other terms are treated implicitly in time. This implies that we store the approximate network velocities on the edge centered grid ($V_n \approx V(R_n^e)$). We impose the boundary condition that $\mathcal{F}_A^{N^+} = -1 \cdot V_0$. Equation (23) for the evolution of strain measure e is treated in an analogous manner. The magnitude of the time step for the entire model is determined by CFL constraints from equations (22) and (23).

Equation (21) which must be solved for the network velocity is elliptic in nature and is thus naturally solved using a finite difference numerical method. On the edge and cell centered grids, we define the standard centered difference operators

$$\mathcal{D}^e f_n = \frac{f(R_n^e) - f(R_{n-1}^e)}{\Delta R} \approx \frac{\partial}{\partial R} f(R_n^c), \quad (40)$$

$$\mathcal{D}^c g_n = \frac{g(R_n^c) - g(R_{n-1}^c)}{\Delta R} \approx \frac{\partial}{\partial R} g(R_{n-1}^e). \quad (41)$$

Applying these operators in place of the derivatives $\frac{\partial}{\partial R}$ in Equation (21), the discrete form of the stress balance equation becomes

$$\frac{2}{R^2} \mathcal{D}^c [R^2 \mathcal{D}^e V] - \frac{4V}{R} = -\mathcal{D}^c [\alpha A^\nu (1 - e) + MA] \quad (42)$$

which is solved directly with the boundary condition that $V(R_N^e) = V_0$.

Rectangular Geometry

We solve the equations on the two dimensional domain $0 \leq x \leq 1$, $0 \leq y \leq 1$. Again, we treat equations (31) and (32) with a finite volume method. However, in this case our control volumes will be square patches. This gives rise to a so called MAC grid with horizontal spacing Δx , vertical spacing Δy and size N_x by N_y [3]. The control volumes are denoted by $\Omega_{i,k}$ and their centers define a cell centered grid

$$\left\{ (x_{i,k}^{\text{cc}}, y_{i,k}^{\text{cc}}) \right\} = \left\{ \left((i - 1/2)\Delta x, (k - 1/2)\Delta y \right) \right\}_{i=1, k=1}^{N_x, N_y} \quad (43)$$

As before, we define

$$A_{i,k} = \frac{1}{|\Omega_{i,k}|} \int_{\Omega_{i,k}} A dV \approx A(x_{i,k}^{\text{cc}}, y_{i,k}^{\text{cc}}). \quad (44)$$

We now average Equation (31) over each control volume, rearrange, and invoke the divergence theorem to give

$$\frac{\partial A_{i,k}}{\partial t} = \frac{|\partial\Omega_{i,k}|}{|\Omega_{i,k}|} \left(\mathcal{F}_A^{(i+1/2,k)} - \mathcal{F}_A^{(i-1/2,k)} + \mathcal{F}_A^{(i,k+1/2)} - \mathcal{F}_A^{(i,k-1/2)} \right) + B - \Gamma A_{i,k}. \quad (45)$$

Here, $\mathcal{F}_A^{(i+1/2,k)}$, $\mathcal{F}_A^{(i-1/2,k)}$, $\mathcal{F}_A^{(i,k+1/2)}$, and $\mathcal{F}_A^{(i,k-1/2)}$ are the fluxes through the right, left, top, and bottom boundaries of $\Omega_{i,k}$ respectively. The above expression has made use of the fact that in the rectangular geometry, these four boundaries of $\Omega_{i,k}$ have the same length. To evolve Equation (45), the flux terms are treated explicitly, while all other terms are treated implicitly in time. The fluxes are again determined with a standard unwinding scheme.

Because of the structure of the discretization in Equation (45), it is advantageous to store the network velocity at the boundary of each control volume. Decomposing the velocity into horizontal and vertical components we see $\vec{V} = u(x, y)\hat{x} + v(x, y)\hat{y}$. Therefore, the horizontal velocity u is stored on the grid which is edge centered in the horizontal direction and cell centered in the vertical direction

$$\left\{ \left(x_{i,k}^{\text{ec}}, y_{i,k}^{\text{ec}} \right) \right\} = \left\{ \left(i\Delta x, (k-1/2)\Delta y \right) \right\}_{i=1, k=1}^{Nx-1, Ny}. \quad (46)$$

Similarly, the vertical velocity v is stored on the grid which is cell centered in the horizontal direction and edge centered in the vertical direction

$$\left\{ \left(x_{i,k}^{\text{ce}}, y_{i,k}^{\text{ce}} \right) \right\} = \left\{ \left((i-1/2)\Delta x, k\Delta y \right) \right\}_{i=1, k=1}^{Nx, Ny-1}. \quad (47)$$

This allows the definition of the discrete gradient operator acts on scalars stored at the cell center grid and produces vectors stored on the edge centered grids

$$\mathcal{G}[f]_{i,k} = \begin{bmatrix} g_1(x_{i,k}^{\text{ec}}, y_{i,k}^{\text{ec}}) \\ g_2(x_{i,k}^{\text{ce}}, y_{i,k}^{\text{ce}}) \end{bmatrix} = \begin{bmatrix} \frac{f(x_{i+1,k}^{\text{cc}}, y_{i+1,k}^{\text{cc}}) - f(x_{i,k}^{\text{cc}}, y_{i,k}^{\text{cc}})}{\Delta x} \\ \frac{f(x_{i,k+1}^{\text{cc}}, y_{i,k+1}^{\text{cc}}) - f(x_{i,k}^{\text{cc}}, y_{i,k}^{\text{cc}})}{\Delta y} \end{bmatrix}. \quad (48)$$

On both edge centered grids, we use the standard five point centered difference discrete Laplacian \mathcal{L} . This leads us to the discrete form of the force balance equation

$$\begin{bmatrix} 0 \\ 0 \end{bmatrix} = \begin{bmatrix} \mathcal{L}u \\ \mathcal{L}v \end{bmatrix} + \mathcal{G}[\alpha A^\nu(1-e) + MA]. \quad (49)$$

This equation is solved directly with Dirichlet boundary conditions.

References

- [1] Pinot, M., V. Steiner, B. Dehapiot, B.-K. Yoo, F. Chesnel, L. Blanchoin, C. Kervrann, and Z. Gueroui, 2012. Confinement induces actin flow in a meiotic cytoplasm. *Proceedings Of The National Academy Of Sciences Of The United States Of America* 109:11705–11710.
- [2] Doghri, I., 2000. Mechanics of deformable solids: linear, nonlinear, analytical and computational aspects. Springer.
- [3] Harlow, F. H., and J. E. Welch, 1965. Numerical Calculation of Time-Dependent Viscous Incompressible Flow of Fluid with Free Surface. *Physics of Fluids* 8:2182.

Location of F-actin maximum density

Center  Edge

α

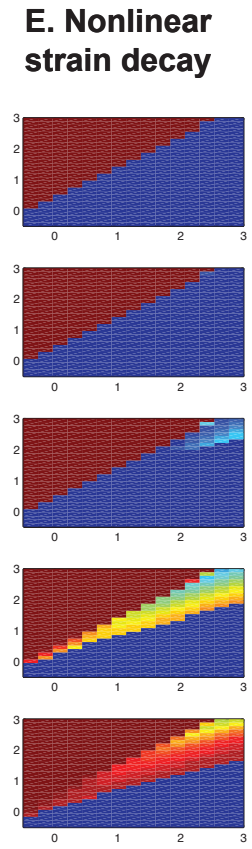
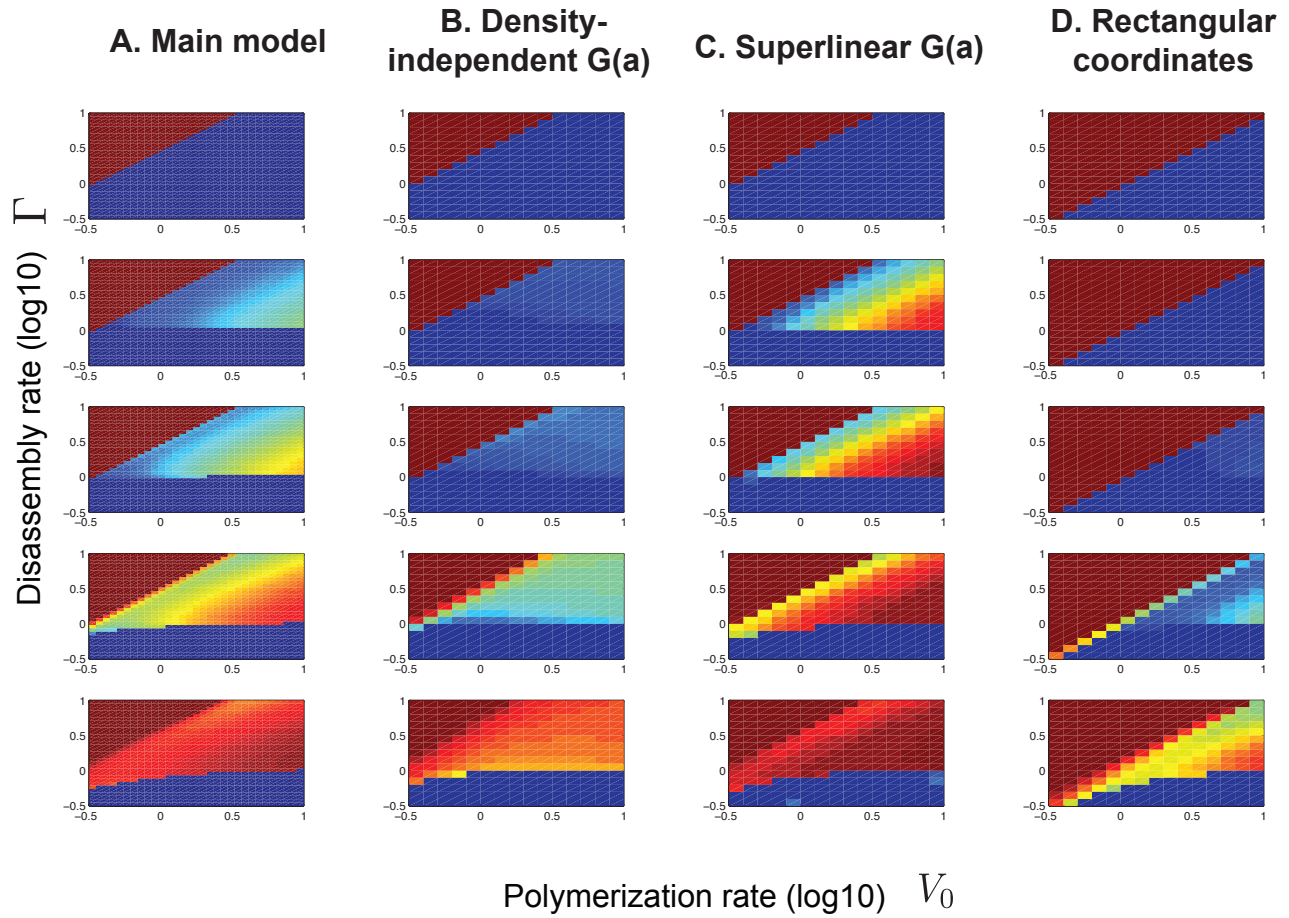
0

0.001

0.01

0.1

1



α

0

0.01

0.1

1

10

(Different axes)